CHAPTER II

Bandwidth enhancement in low-profiled SIW integrated E- shaped patch antenna array with inbuilt calibration lines

2.1. Introduction

2.2. Design and simulated performance

2.2.1. SIW integrated unit antenna element

2.2.2. Analysis of the SIW integrated E-shaped element in array environment

2.2.3. Inbuilt calibration line in 2×8 antenna array

2.2.4. 8×8 antenna array with inbuilt calibration line

2.2.5. Simulated scan performance of 8×8 antenna array with calibration line

2.3. Implementation and performance evaluation

2.3.1. Fabrication of the proposed 8×8 antenna array with inbuilt calibration line

2.3.2. Performance study of the fabricated antenna array

2.4. Summary

2.1. INTRODUCTION

Wide bandwidth is an essential ECCM (Electronic Counter-Counter Measures) feature for modern phased array radar. When designing and developing these antenna arrays, careful consideration should be given to the antenna element selection, keeping in mind the Phased Array Antenna (PAA) performance specifications [1]. As mentioned in Chapter I, microstrip patch antennas are the best candidate for constructing an array. A low dielectric constant substrate with low loss tangent is ideal for designing high-efficiency patch antennas, nevertheless, this narrows the band width. Using a thicker substrate, do enhances the bandwidth, but on hindsight generates unwanted surface wave propagation and also increases the form factor of the array. Substrate Integrated Waveguide (SIW) technique has been used for overcoming narrow impedance bandwidth in the patch antennas [2-7]. Ease of implementation, quick prototyping and accurate manufacturing of SIW structures have successfully made its way into incorporation in tile-based active phased array architectures [8].

Antenna arrays in PAAs are generally powered by Transmit/Receive (T/R) modules, which are made of active elements. Over the time, the active element's response quality deteriorates, which has an immediate impact on its performance [9]. From time to time calibration of T/R modules are required. Reported calibration techniques mainly involve the use of external near-field/far-field probe scanning around the perimeter of the array to determine the relative phase and amplitude of each antenna element [10-17]. Alternatively, in peripheral probe scanning method, one or more probes are fixed around the edge of the phased array and the coupling between antennas is quantified and excitation errors are accounted [18]. However, this works best for the phased array's initial factory calibration and is not conducive to frequent in-field calibration. A more acceptable approach to calibrating PAA is the Mutual Coupling Calibration Method (MCCM) [19]. The MCCM technique involves measuring the mutual coupling between the adjacent antenna elements and should be identical to the factory settings. The array is initially aligned with factory settings and then re-calibrated in the field. The accuracy of this technique, however, is limited for low-powered T/R modules and often requires complex calibration algorithms [20].

In this chapter, a hybrid approach of amalgamating SIWs and slotted patch is carried out to achieve wideband for a 64-element patch antenna array in X-band. Unit structure of the array is an E-shaped patch, giving advantages whilst improved bandwidth, relatively simple design, and with the two E-arms giving wider options for manipulating frequencies of operation [21]. An inbuilt printed calibration lines are included in the array design.
The design is optimized and tested for centre element impedance and radiation characteristics measured in presence of the calibration lines. CST Microwave studio is used for all the design and optimization.

2.2. DESIGN AND SIMULATION

2.2.1. SIW integrated unit antenna element

The unit antenna element is designed to operate at a resonance frequency of 8.75 GHz. The antenna is intended for integration into a planar array, hence, the dimensions of the ground plane in the x and y directions are governed by Equation 2.1 [22], to prevent the occurrence of grating lobes within the visible range,

$$\boldsymbol{d_{max} < \frac{\lambda_F}{1 + |\sin\theta_{max}|}} \qquad (2.1)$$

where, d_{max} is the maximum interelement spacing, λ_F is the free-space wavelength of the highest frequency of operation, and θ_{max} is the maximum scanning angle. The dimensions, $W \times L$ thus found are $0.51\lambda_0 \times 0.49\lambda_0$, where λ_0 is the free-space wavelength corresponding to the centre frequency.

Initially an E-shaped metallic patch is fabricated on a Rogers 5880LZ substrate with a thickness of 1.27 mm, relative permittivity, $\varepsilon_r = 2$, and loss tangent, $tan\delta = 0.002$, as described in Figure 2.1(a). The patch length, L_p, and width, W_p, are determined using the transmission line model (TLM) technique as detailed in [22]. The simulated return loss behaviour of E-patch antenna is shown in Figure 2.1(b). The antenna has a -10 dB bandwidth of 340MHz extending from 8.36-8.70 GHz.

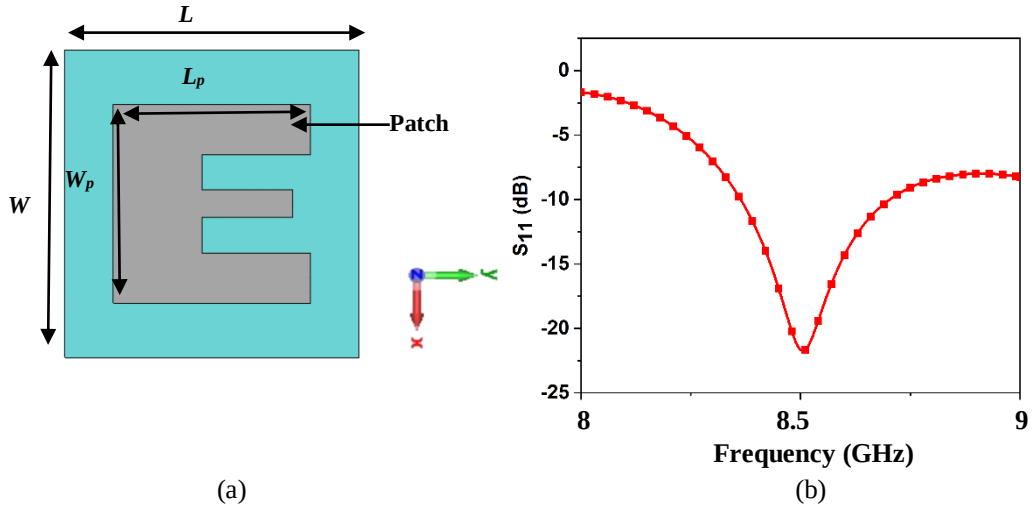

(a) (b)

Figure 2.1 (a) Initial design of E- shaped patch antenna. (b) Simulated return loss, S_{11}, of the E- shaped patch antenna.

The return loss performance of the E-shaped patch is further improved by introducing slots in its upper and lower arms and a pair of slots in the non-radiating edge. Substrate integrated waveguide (SIW) isolators are placed around the patch which comprises of metallized vias connected to the ground plane of the antenna through the substrate as illustrated in Figure 2.2(a). The vias of diameter D is placed distance s apart, as shown in inset Figure 2.2(a), and are connected to each other by a metal plate of width, w. In order to make the SIW cavity equivalent to a conventional metallic cavity, the conditions to be fulfilled are $\frac{D}{s} \geq 0.5$ and $\frac{D}{\lambda o} \leq 0.1$ [23]. The values of D and s are set accordingly. The exploded view of different layers of the antenna is shown in Figure 2.2(b). The antenna is fed using coaxial ports at a point of 50 Ω impedance matching. The optimized design parameters are written in Table 2.1.

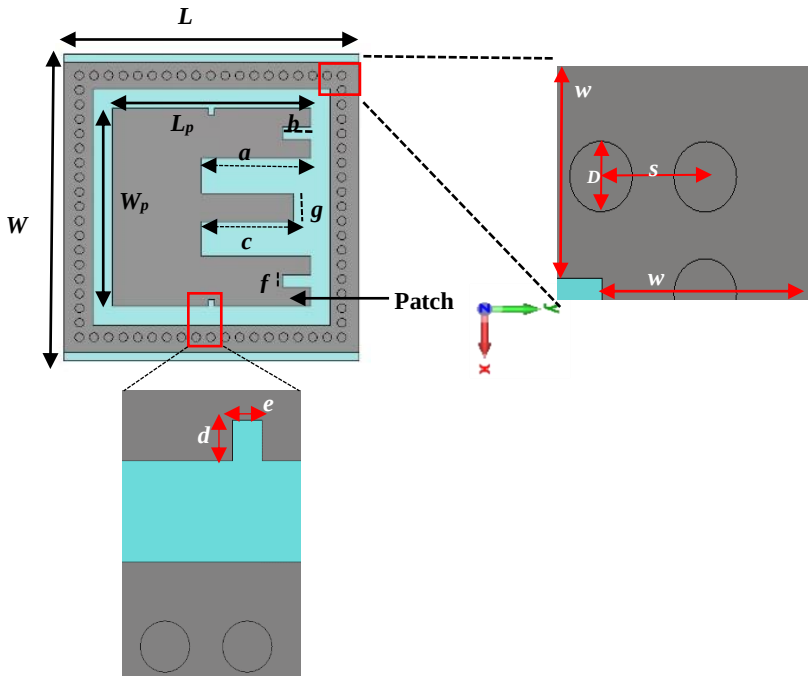

(a)

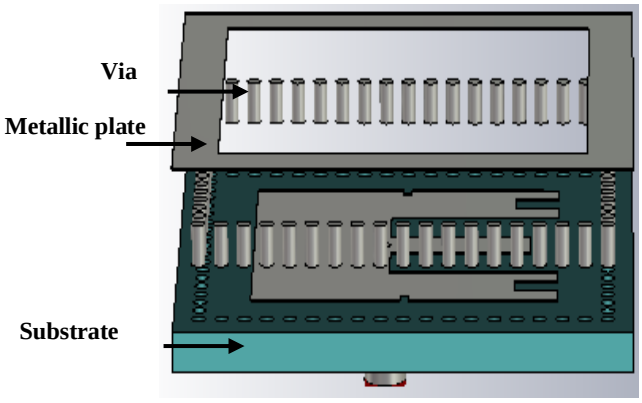

(b)

Figure 2.2 SIW incorporated slotted E-shaped single antenna element, (a) structure with vias with insets showing expanded view of vias and slot and (b) exploded lateral view

Table 2.1 Parameters of SIW integrated slotted E-shaped single antenna element

Parameters	***L***	***W***	L_p	W_p	***a***	***b***	***g***
Dimensions (mm)	16.80	17.50	11.26	11.32	6.2	1.2	1.6
Parameter	***c***	***d***	***e***	***w***	***D***	***s***	***f***
Value (mm)	5.2	0.4	0.3	1.65	0.5	0.83	0.9

SIW incorporated slotted E-shaped antenna element shows -10dB bandwidth of 500 MHz, as seen in Figure 2.3(a). The radiation pattern at the centre frequency of 8.75 GHz in H- and E-planes are plotted in Figure 2.3(b). A simulated gain of 7.3 dB in H-plane and 7.32

dB in E-plane with a 3dB beam width of 83.7° in H-plane and 83.4° in E-plane are observed. The simulated efficiency of the antenna element is above 90% in the operating band as indicated in Figure 2.3(c). The intensity of interelement coupling for the two scenarios, viz. without (WO) and with (W) SIWs are shown in Figure 2.3(d and e) respectively. As indicated in the figure, the surface currents are confined within the SIW and metallic plate boundary, indicating reduction in its spreading to the nearby patch. The mutual coupling plots in Figure 2.3(f), for WO_SIW and W_SIW shows a reduction of 2.02 dB in its value at 8.75GHz.

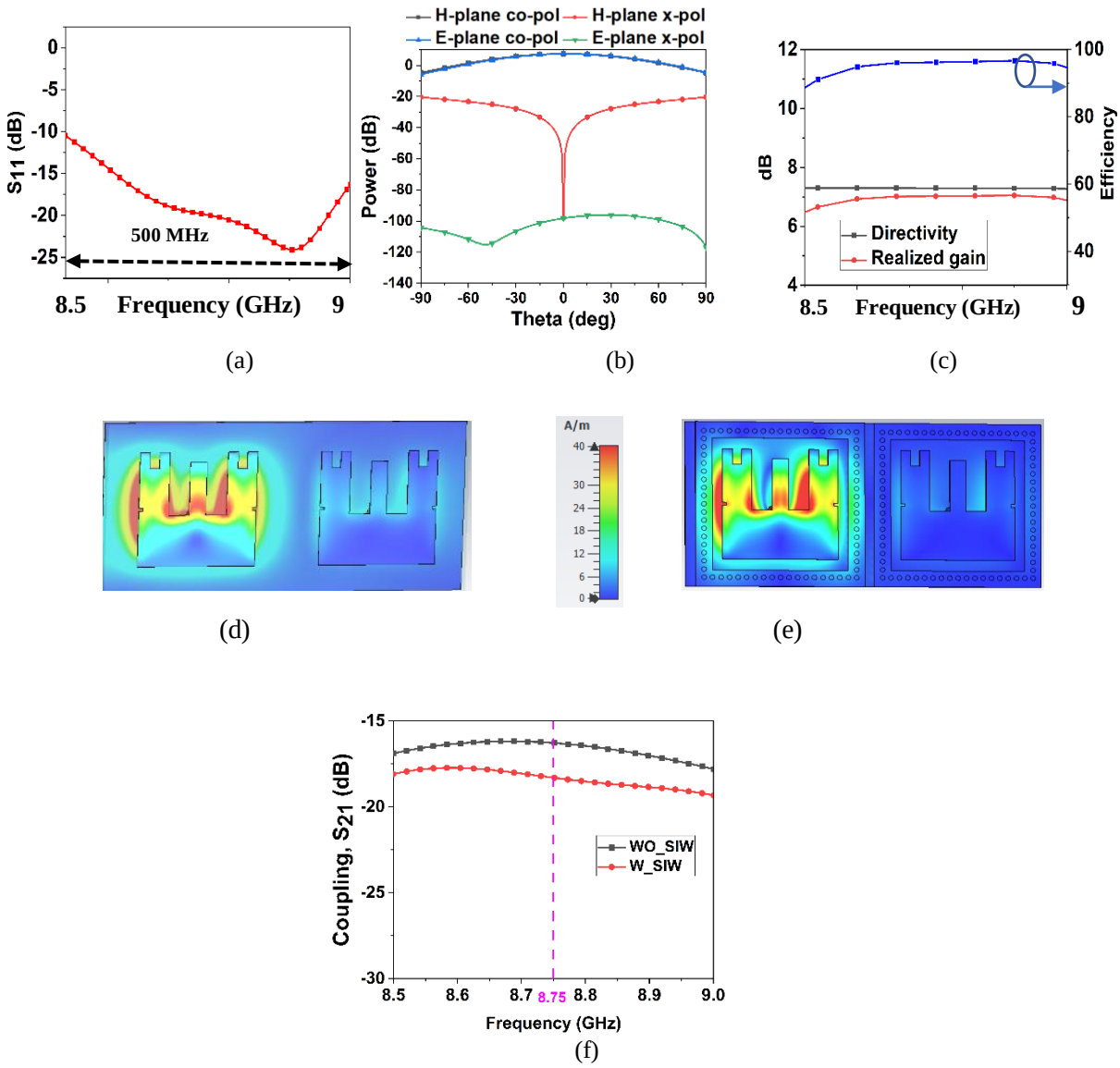

(a) (b) (c)

(d) (e)

(f)

Figure 2.3 Slotted E-shaped single element simulated (a) S_{11} (b) radiation pattern, (c) efficiency. (d) Surface current distribution (d) without SIWs and (e) with SIWs. (f) Coupling (S_{21}) between the antennas for the case without (WO) and with (W) SIWs.

2.2.2. Analysis of the SIW integrated E-shaped element in array environment

A full Floquet port boundary conditions are implemented to study the active return loss (ARL) for different scan orientations for both the orthogonal planes in the array environment as shown in Figure 2.4(a). The Finite Element Method (FEM) solver is used in conjunction with a curved tetrahedral mesh. Scanning angles are varied in steps of 10° in both H- and E-planes and the simulated active return loss is drawn in Figure 2.4(b and c). ARL of -10 dB is achieved for scan angles up to $\pm 50°$ in H-plane and $\pm 60°$ in E-plane, beyond which the ARL deteriorates.

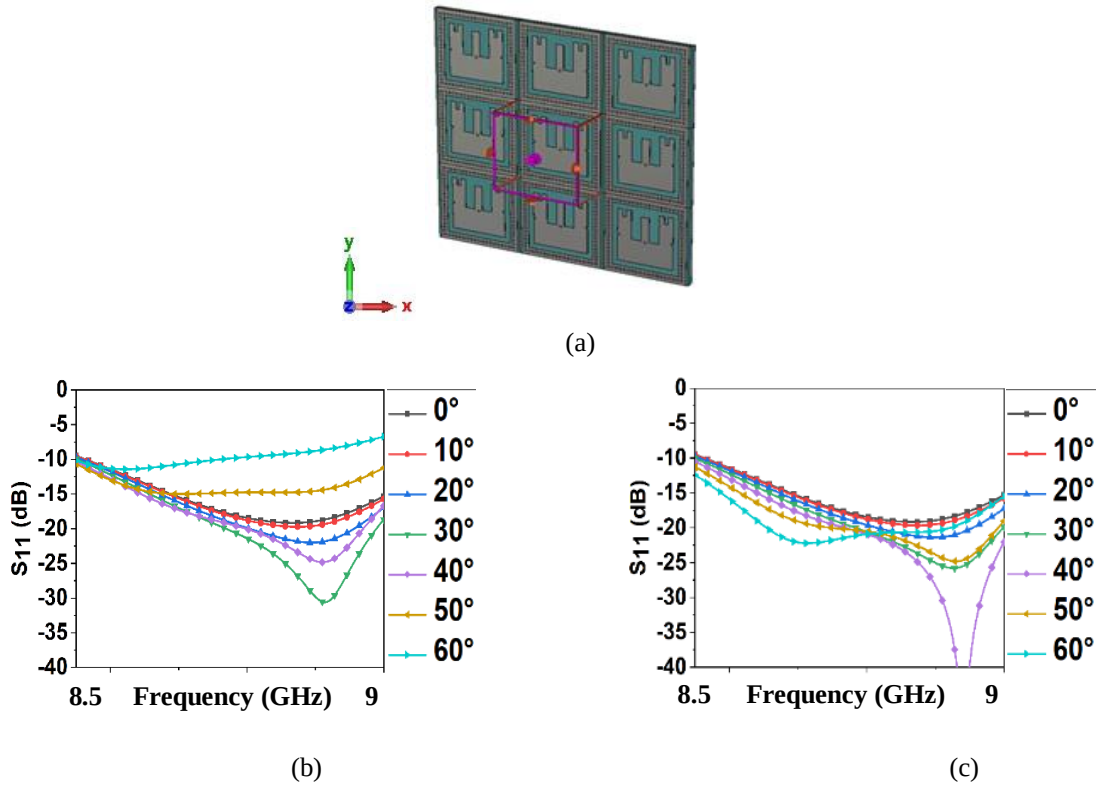

Figure 2.4. Simulated for with centre element excited in array environment (a) model of periodic boundary condition, and ARL at different scan in (b) H-plane and (c) E-plane.

2.2.3. 2×8 antenna array with inbuilt calibration line

The single antenna studied in Section 2.2.2 is extended along x and y directions to form a 2×8 array. A 100Ω calibration line of width $0.42\ mm$ is drawn in between the antenna elements parallel to the non-radiating edge at a gap of 0.3 mm from the SIW isolators. The line is placed so as to not affect the integrity of the SIW framing. The width is selected

considering the space constrains between the antenna elements in the proposed array. The schematic representation of the calibration line is shown in Figure 2.5. The 100 Ω line impedance is matched to the 50 Ω line through a quarter wave transformer as shown in inset of Figure 2.6(a). The coupling values, S_{xy} is measured between the antenna elements and the calibration lines, where x is the antenna port and y is the calibration line port. The design of the line is optimized to maintain S_{xy}within -30 dB to -40 dB considering sensitivity of T/R module. The coupling values from different antenna elements to calibration port is measured by exciting one of the ports (*say port 17*) of the calibration line and one of the antenna elements at a time while terminating all the remaining ports with a 50Ω matched load, as represented in Figure 2.6(a). This technique assists in identifying which T/R module corresponding to the element has deviated from its factory settings of amplitude and phase. The dynamic range of S_{xy} is below 9dB in the frequency range 8.5-9 GHz. At the centre frequency, S_{xy} ranges between -34.4 dB to -37.3 dB as seen from Figure 2.6(b).

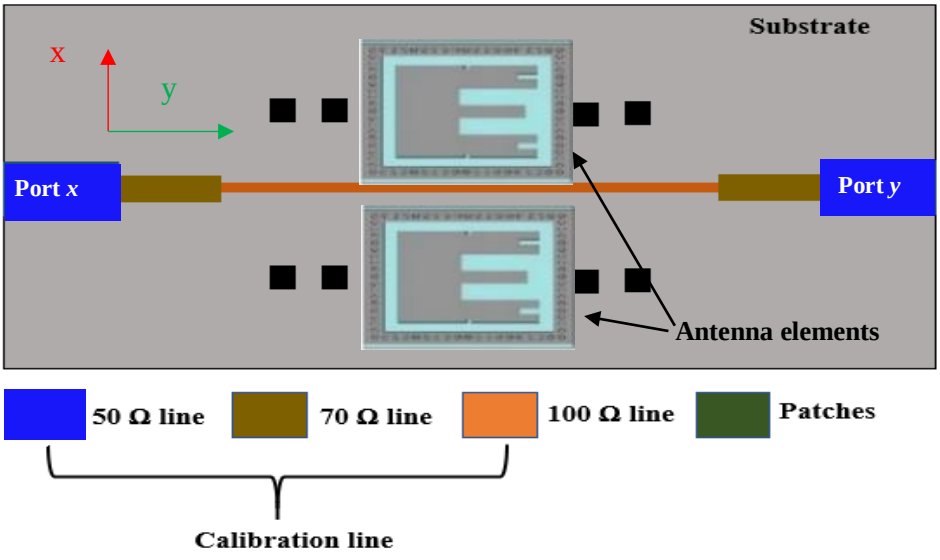

Figure 2.5. Schematic representation of calibration line placement in the array.

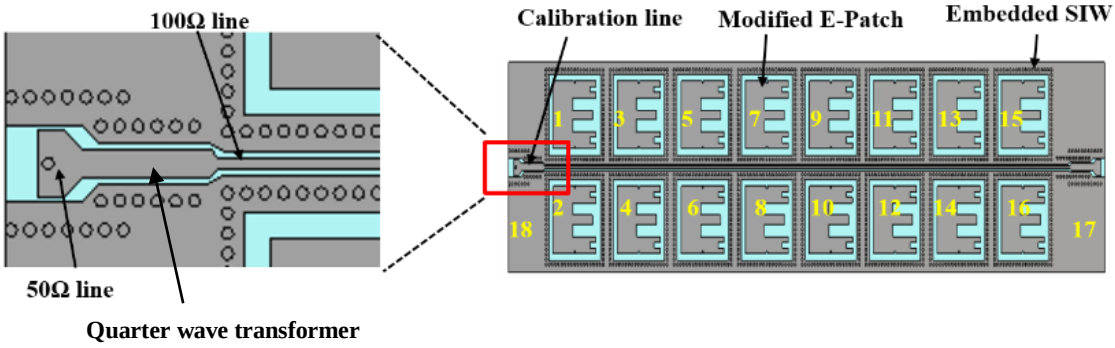

(a)

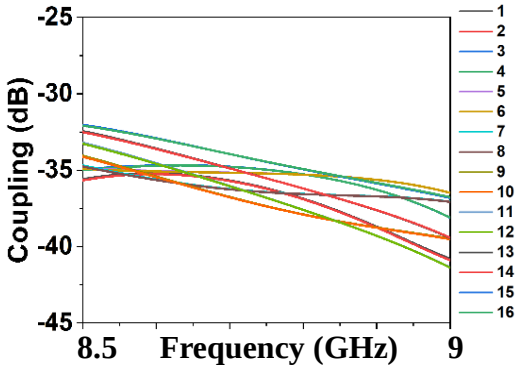

(b)

Figure 2.6. (a) Inset quarter wave transformer connecting 50 Ω port to 100 Ω calibration line. (b) Schematic for measuring coupling values. (c) Simulated coupling values between different elements and calibration line.

2.2.4. 8 × 8 antenna array with inbuilt calibration line

2 × 8 array system with inbuilt calibration line mentioned in Section 2.2.3 is expanded to 8 × 8 array in a tile-based grid, as shown in Figure 2.7(a). All the 64 elements are individually connected to coaxial port. The dimension of the 8 × 8 array with calibration lines is placed in Table 2.2. Initially only the central element of the array is excited, as indicated by the red square in Figure 2.7(a), while all the other elements are terminated in matched load. Figure 2.7(b) plot shows that the return loss improves and a -10dB bandwidth > 500 MHz. A minimum isolation of 15 dB and 21 dB is obtained in H- and E-plane respectively.

The active element pattern is a crucial factor in shaping the overall performance of a large phased array system. It influences key aspects such as the array's radiation pattern, peak gain in a specific scan direction, cross-polarization levels and active reflection coefficient

magnitude of a fully excited array. This pattern is determined by activating a single radiating element while ensuring that all the other elements are properly matched. The simulated radiation patterns are considered for the three frequencies viz. 8.5 GHz (F_L), 8.75 GHz (F_C) and 9 GHz (F_H). The simulated H- and E-planes active element radiation patterns are shown in Figure 2.7(c and d). The realized gain of the centre element varies from 4.46 to 5.39 dBi over the whole operational band. The normalized cross-polarization levels are below 30 dB in both H- and E-planes in the broadside direction. Simulated -3 dB beam width and realized gain of the centre element, is tabulated in Table 2.3.

Figure 2.7(e) depicts the 8×8 array's simulated realized gain pattern in the broadside direction with all the 64 elements excited. A peak gain of 23 dBi and cross-polarization of maximum 42.5 dB in H-plane and 51 dB in E- plane is observed at 8.75 GHz. Low thickness of the substrate $(0.036\lambda o)$, enables the structure to achieve a low cross-polarization level which is similar to that observed in reference [24].

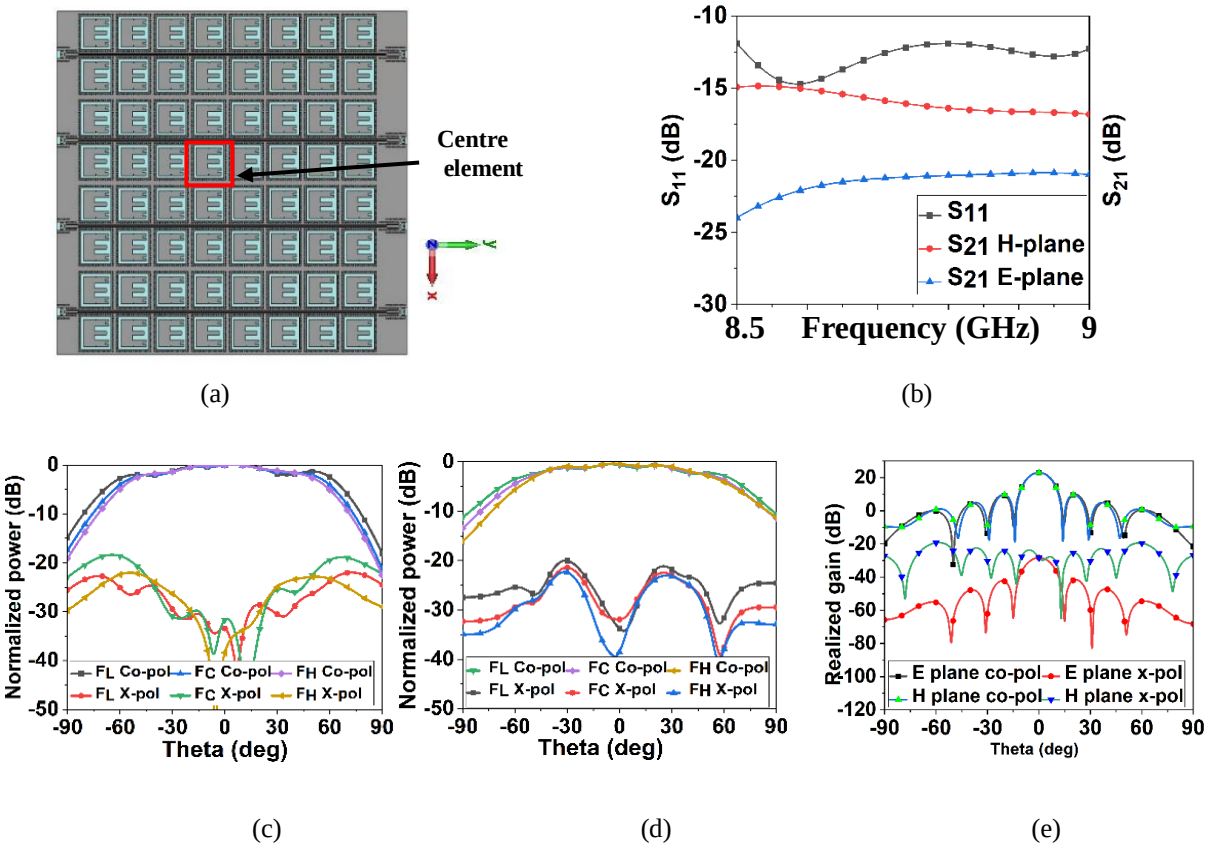

(a) (b)

(c) (d) (e)

Figure 2.7. (a) Design of 8×8 planer array. (b) Simulated S_{11} and S_{21} of the centre element in E- and H-plane. Simulated normalized centre element radiation pattern at F_L, F_C and F_H in (c) H-plane and (d) E-plane. (e) Simulated broadside gain pattern with simultaneous excitation of all the elements of the array.

Table 2.2. Optimized parameters of the 8×8 antenna array with the calibration line

Parameters	Dimension (mm)
Length of array, L	150
Width of the array, W	153
Thickness of the 50Ω line	2.8
Thickness of the 70Ω line	1.28
Thickness of the 100Ω line	0.4

Table 2.3. Simulated -3dB beam width (BW) and gain of the centre element of array

Frequency (GHz)	E-plane		H-plane	
	-3 dB Beam width	Gain (dB)	-3 dB Beam width	Gain (dB)
8.5	120.7°	4.81	123.6°	4.46
8.75	109.1°	5.38	112.1°	5.18
9.0	101.8°	5.51	105.4°	5.39

2.2.5. Simulated scan performance of 8×8 antenna array with calibration line

The phase shifts in x and y directions for different scan directions are determined using Equations 2.2(a and b) [22].

$$\beta_x = -kd_x sin\theta_o cos\varphi_o \qquad (2.2a)$$

$$\beta_y = -kd_y sin\theta_o sin\varphi_o \qquad (2.2b)$$

where, φ_o represents the direction of major lobe in azimuth and θ_o represents the major lobe direction from the zenith. β_x and β_y are corresponding phase shifts in x and y directions, $k = \frac{2\pi}{\lambda}$, and the inter-element distance in the x and y directions are designated by d_x and d_y respectively. The normalized simulated scanning pattern of the array in both the H-plane and E-plane at three different frequencies viz. 8.5 GHz, 8.75 GHz and 9 GHz are shown in Figure 2.8 and 2.9 respectively. Maximum scan angle of 50° is achieved in H-plane and 60° in the E-plane without any grating lobes.

On simultaneously exciting all the elements of the array, the side lobe level (SLL) in the H-plane at $\theta = 50°$ for 8.5 GHz excitation, is -12.61 dB and at 9 GHz is -12.81 dB. In the

E-plane, the SLL at $\theta = 60°$ for 8.5 GHz, is -13.3 dB and for 9 GHz is -12.97 dB. The array at 8.5 GHz exhibits a maximum scan loss of -1.81 dB in the H-plane (at $\theta = 50°$) and -3.1 dB in the E-plane ($\theta = 60°$), whereas when the array excited at 9GHz, a maximum scan loss of -2.17 dB in the H-plane and -5.1 dB in the E-plane is observed.

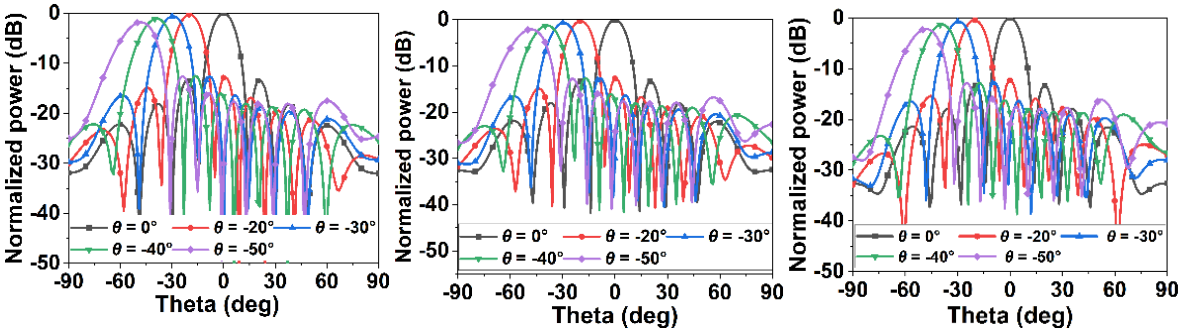

(a) (b) (c)

Figure 2.8. Normalized simulated scanning patterns at (a) 8.5 GHz, (b) 8.75 GHz, (c) 9 GHz in H-plane.

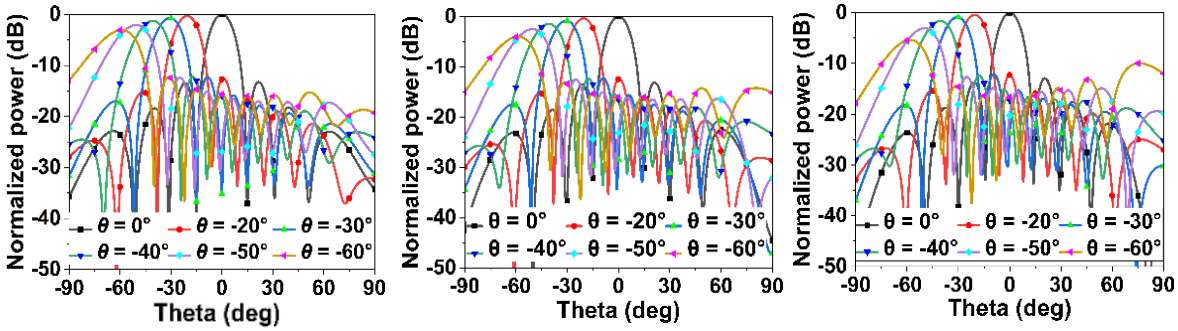

(a) (b) (c)

Figure 2.9. Normalized simulated scanning patterns at (a) 8.5 GHz, (b) 8.75 GHz, (c) 9 GHz in E-plane.

2.3. IMPLEMENTATION AND PERFORMANCE EVALUATION

2.3.1. Fabrication of the proposed 8×8 antenna array with inbuilt calibration line

The 64-element array with inbuilt calibration lines with dimensions mentioned in Table 2.2 is fabricated using photolithography technique. SIWs are constructed using plated-through-hole (PTH) technique. The top view of the fabricated array is shown in Figure 2.10(a). The magnified view of the radiating E-patch antenna element is drawn in inset of Figure 2.10(b). Enlarged view of the calibration line connection to the (Subminiature A) SMA connector is shown in Figure 2.10(c). The array is fastened to an aluminum plate with threaded holes

to connect the SMP (Subminiature Push-on) connector as shown in Figure 2.10(c). A Vector Network Analyzer (Agilent Technologies N5242A) is used to measure the return loss and the coupling values. The red rectangular box outlined in the Figure 2.10(a) indicates the 2 × 8 antenna array considered for measuring the coupling coefficients at the calibration port for validation of the calibration line design.

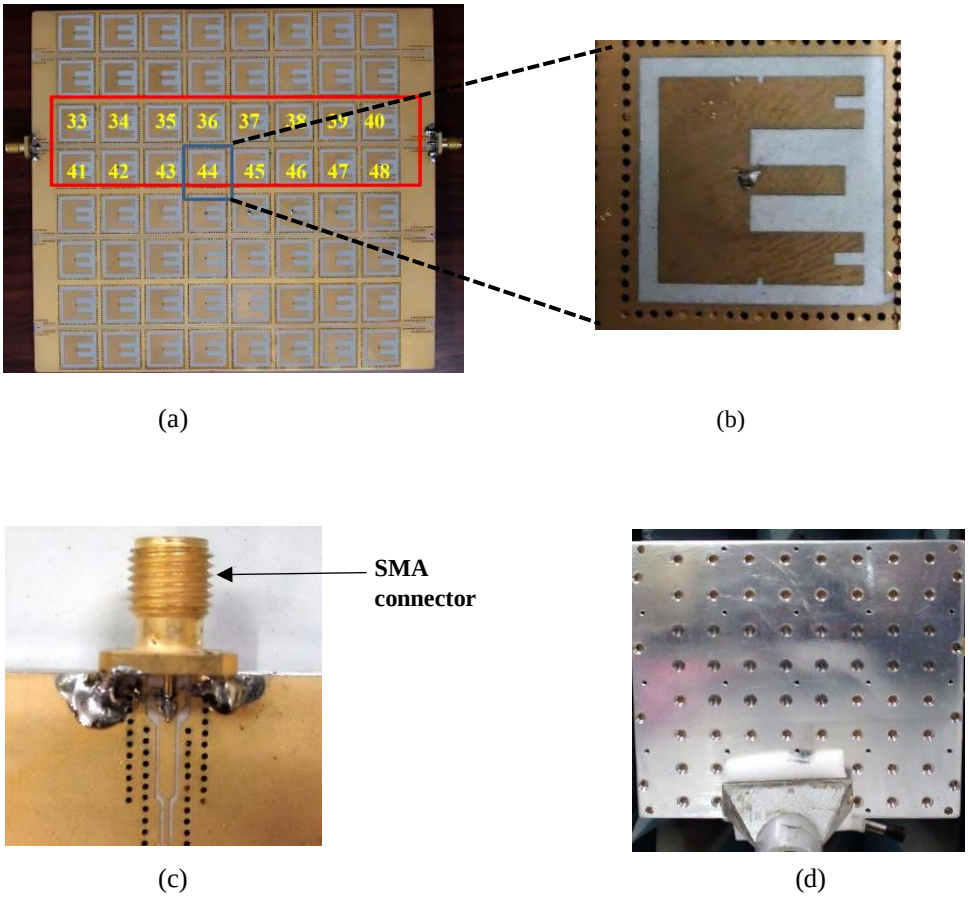

Figure 2.10. (a) Fabricated 8×8 array top view. (b) Inset showing expanded view of SIW integrated slotted E-shaped antenna element. (c) Magnified view of calibration line termination with SMA connector. (d) Rear view of the array.

2.3.2. Performance study of the fabricated antenna array

Figure 2.11(a) indicates the coupling coefficient between the calibration line and the antenna elements. A dynamic range of 15dB between 8.5-9.0 GHz and 9 dB at 8.75 GHz is seen in the coupling coefficients. Some difference in the coupling values as compared to simulation plots in Figure 2.6(b), might be due to the fabrication and soldering tolerances. All the elements of the array are attached with SMP connectors for measuring the centre

element return loss. The measured return loss and the coupling values with the centre element excited in the 8×8 array is shown in Figure 2.11(b). Comparing with Figure 2.7(b) and 2.11(b), the simulated and measured result of the S_{11} and S_{21} with the centre element excited, a similar trend is observed. Fabricated array has a total impedance bandwidth of 7.95% covering more than 500 MHz.

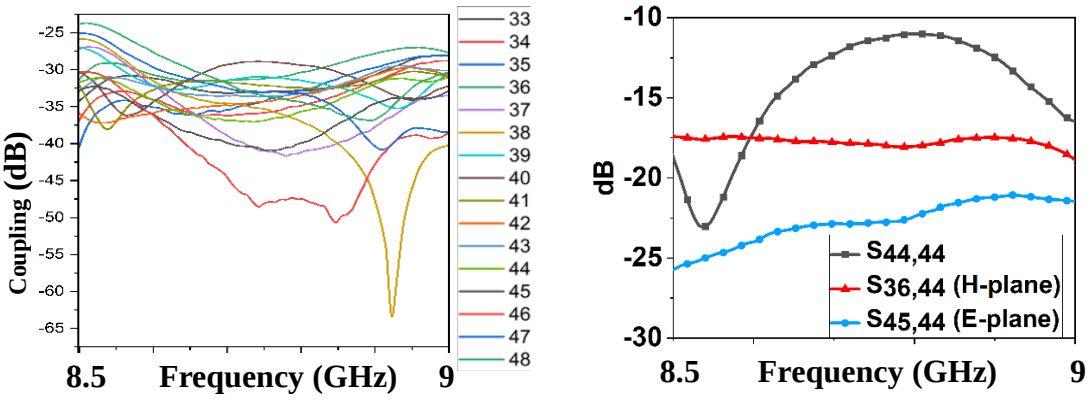

(a) (b)

Figure 2.11. Measured (a) coupling coefficients at the calibration port (b) return loss and coupling with only centre element excited.

The 2-D active element radiation pattern is measured in Planar Near Field Measurement (PNFM) facility of LRDE DRDO, with only the centre element of the array excited. Figure 2.12(a) shows the radiation pattern measurement setup of the array where a waveguide probe is used to capture the nearfield energy around the array which is then converted to far field radiation pattern using standard near field to far field data plotting algorithms. The H- and E-plane radiation patterns of the central element is measured over the frequency bandwidth at 8.5 GHz (F_L), 8.75 GHz (F_C) and 9 GHz (F_H) and is presented in Figure 2.12(b and c). Broadside cross-polarization levels in the measured active element pattern are below -20 dB in both H- and E-plane, respectively. The 3dB beam width range fluctuations are less than -2 dB for both H- and E-planes. The comparison between simulated and measured gain levels and measured efficiency of the centre element of the array is drawn in Figure 2.12(d). Table 2.4 lists the measured and simulated -3 dB beam widths, with only the centre element excited, in both the planes.

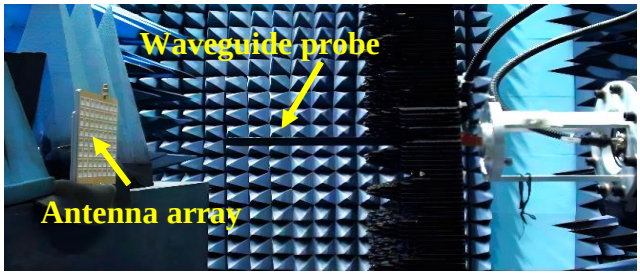

(a)

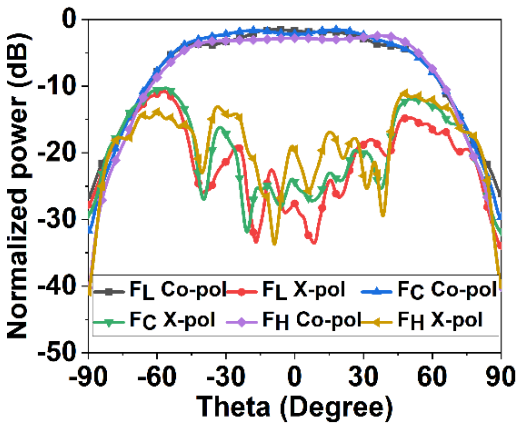

(b)

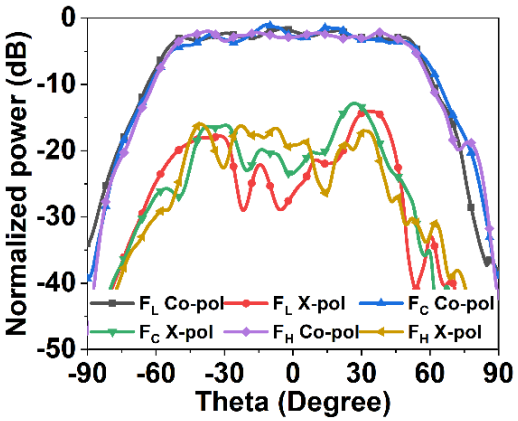

(c)

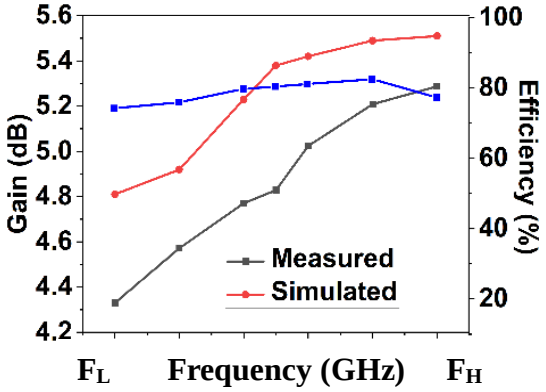

(d)

Figure 2.12. (a) Radiation pattern measurement setup. Measured radiation pattern with only centre element excited in (b) H-plane and (c) E-plane. (d) Simulated and measured gain and efficiency.

Table 2. 4 Simulated and measured -3 dB beam width of centre element of the array

Frequency (GHz)	E-plane (deg)		H-plane (deg)	
	Simulated	**Measured**	**Simulated**	**Measured**
8.5	120.7	110.7	123.6	114.7
8.75	109.1	104.1	112.1	112.09
9	101.8	103.8	105.4	107.2

As seen from Table 2.4, a similarity in the simulated and measured -3 dB beam width is observed for the centre element of the array. In simulation only SMP connectors are considered, whereas in measurements the SMP-SMA adapters are used, which may lead to variance in results.

2.4. CHAPTER SUMMARY

This chapter presents an 8×8 patch antenna array that demonstrates several important characteristics for practical phased array applications. The array features a low-profile design of approximately 0.036λo, ensuring ease of manufacturing, integration, and transportation. It exhibits a wide impedance bandwidth of 7.95% in the X-band, making it suitable for broadband operation. The array supports wide beam scanning with coverage of ±50° in both the azimuth and elevation planes, providing flexible directional control. To enhance field usability, inbuilt calibration lines are incorporated, enabling fast on-site calibration without reliance on external near- or far-field probes. This self-calibration capability significantly improves the reliability and adaptability of the system in real-world scenarios. Furthermore, the measured results confirm a cross-polarization level better than 20 dB in both orthogonal planes for the center element of the array, ensuring stable polarization purity and high-quality radiation performance.

References

[1]. Fourikis, N.: Phased array-based systems and applications. *Wiley*, New York, 1997.

[2]. Ng, K. B., Wong, H., So, K. K., Chan, C. H., Luk, K. M. 60 GHz plated through hole printed magneto-electric dipole antenna. *IEEE Transactions on Antennas and Propagation*, 60(7):3129–3136, 2012. DOI: 10.1109/TAP.2012.2196917

[3]. Li, M., Luk, K. Wideband magneto-electric dipole antenna for 60-GHz millimeter-wave communications. *IEEE Transactions on Antennas and Propagation*, 63(7):3276–3279, 2015. DOI: 10.1109/TAP.2015.2429684

[4]. Li, Y., Luk, K. A 60-GHz wideband circularly polarized aperture coupled magneto-electric dipole antenna array. *IEEE Transactions on Antennas and Propagation*, 64(4):1325–1333, 2016. DOI: 10.1109/TAP.2016.2528227

[5]. Ruan, X., Qu, S., Zhu, Q., Ng, K. B., Chan, C. H. A complementary circularly polarized antenna for 60-GHz applications. *IEEE Antennas and Wireless Propagation Letters*, 16:1373–1376, 2017. DOI: 10.1109/LAWP.2016.2633543

[6]. Zhu, Q., Ng, K. B., Chan, C. H., Luk, K.-M. Substrate-integrated waveguide-fed array antenna covering 57–71 GHz band for 5G applications. *IEEE Transactions on Antennas and Propagation*, 65(12):6298–6306, 2017. DOI: 10.1109/TAP.2017.2755440

[7]. Alibakhshikenari, M., Virdee, S. B., Salekzamankhani, S., et al. High-isolation antenna array using SIW and realized with a graphene layer for sub-terahertz wireless applications. *Scientific Reports*, 11(1):87712, 2021. DOI: 10.1038/s41598-021-87712-2

[8]. Kamalzadeh, S., Arand, B. A. Patch array antenna with cavity-backed SIW feed for X-band applications. *Microwave and Optical Technology Letters*, 58(2):319–323, 2016. DOI: 10.1002/mop.29524

[9]. He, G., Gao, X., Zhang, R. Impact analysis and calibration methods of excitation errors for phased array antennas. *IEEE Access*, 9:59010–59026, 2021. DOI: 10.1109/ACCESS.2021.3072683

[10]. Litschke, O., Simon, W., Holzwarth, S. A 30 GHz highly integrated LTCC antenna element for digital beam forming arrays. *IEEE Antennas and Propagation Society International Symposium Digest*, pp. 297–300, 2005.

[11]. Passmann, C., Hickel, F., Wixforth, T. Investigation of a calibration concept for optimum performance of adaptive antenna systems. *Proceedings of the IEEE 48th Vehicular Technology Conference*, pp. 577–580, 1998. DOI: 10.1109/VETEC.1998.686588

[12]. Takeuchi, Y., Hirayama, H., Fukino, K., Murayama, T., Notsu, Y., Hayashi, A. Auto calibrated distributed local loop configuration of array antenna for CDMA cellular base station. *Proceedings of the IEEE 6th International Symposium on Spread Spectrum Techniques and Applications*, pp. 666–670, 2000. DOI: 10.1109/ISSSTA.2000.882051

[13]. Nuteson, T. W., Stocker, J. E., Clark, J. S., Haque, D. S., Mitchell, G. S. Performance characterization of FPGA techniques for calibration and beamforming in smart antenna applications. *IEEE Transactions on Microwave Theory and Techniques*, 50(12):3043–3051, 2002. DOI: 10.1109/TMTT.2002.805178

[14]. Agrawal, A., Jablon, A. A calibration technique for active phased array antennas. *Proceedings of the IEEE International Symposium on Phased Array Systems and Technology*, pp. 223–228, 2003. DOI: 10.1109/PAST.2003.1246663

[15]. Gao, T., Gou, Y., Wang, J., Chen, X. Large active phased array antenna calibration using MCM. *IEEE Antennas and Propagation Society International Symposium Digest*, pp. 606–609, 2001.

[16]. Ji, Y., Nielsen, J. Ø., Fan, W. A simultaneous wideband calibration for digital beamforming arrays at short distances. *IEEE Antennas and Propagation Magazine*, 63(3):102–111, 2021. DOI: 10.1109/MAP.2020.3048503

[17]. Long, R., Ouyang, J., Yang, F., Han, W., Zhou, L. Fast amplitude-only measurement method for phased array calibration. *IEEE Transactions on Antennas and Propagation*, 65(4):1815–1822, 2017. DOI: 10.1109/TAP.2017.2671460

[18]. Stark, A., Rohrdantz, B., Johannsen, U., Jacob, A. F. In-situ probes for patch antenna array calibration. *International Journal of Microwave and Wireless Technologies*, 3(3):273–280, 2011. DOI: 10.1017/S1759078711000160

[19]. Bekers, D., van Dijk, R., van Vliet, F. Mutual-coupling based phased-array calibration: A robust and versatile approach. *Proceedings of the IEEE*

International Symposium on Phased Array Systems and Technology, pp. 1–6, 2014. DOI: 10.1109/ARRAY.2014.7012724

[20]. Yang, L., Dang, R., Li, M., Zhao, K., Song, C., Xu, Z. A fast calibration method for phased arrays by using the graph coloring theory. *Sensors*, 18(12):4315, 2018. DOI: 10.3390/s18124315

[21]. Gopal, M., Ray, K. P. Design of 16x16 Phased Array Antenna for X-band Radar. *2022 3rd International Conference for Emerging Technology (INCET)*, Belgaum, India, pp. 1–6, 2022. DOI: 10.1109/INCET54531.2022.9824702

[22]. Balanis, C. A. *Antenna Theory: Analysis and Design*. John Wiley & Sons, 4th ed., 2016.

[23]. Luo, G. Q., Wang, T. Y., Zhang, S. Review of low-profile substrate integrated waveguide cavity backed antennas. *International Journal of Antennas and Propagation*, 2013:1–7, 2013. DOI: 10.1155/2013/462957

[24]. Huag, J., Zhang, X., Xie, S., Wu, W., Yuan, N. Suppression of cross-polarization of the microstrip integrated balun-fed printed dipole antenna. *International Journal of Antennas and Propagation*, 2014:1–8, 2014. DOI: 10.1155/2014/319632